Inorganic Chemistry

Article

Cite This: *Inorg. Chem.* 2019, 58, 14853−14862

pubs.acs.org/IC

Average and Local Structure of Apatite-Type Germanates and Implications for Oxide Ion Conductivity

Matthew S. Chambers,[†,‡] Philip A. Chater,[‡] Ivana Radosavljevic Evans,*[,†] and John S. O. Evans*[,†]

[†]Department of Chemistry, Durham University, South Road, Durham DH1 3LE, United Kingdom

[‡]Diamond Light Source, Diamond House, Harwell Science and Innovation Campus, Didcot OX11 0DE, United Kingdom

Supporting Information

ABSTRACT: Materials with the apatite structure have a range of important applications in which their function is influenced by details of their local structure. Here, we describe an average and local structural study to probe the origins of high-temperature oxide ion mobility in $La_{10}(GeO_4)_6O_3$ and $La_8Bi_2(GeO_4)_6O_3$ oxygen-excess materials, using the low-conductivity interstitial oxide-free $La_8Sr_2(GeO_4)_6O_2$ as a benchmark. For La_{10} and La_8Bi_2, we locate the interstitial oxygen, O_{int}, responsible for conductivity by Rietveld refinement and relate the $P6_3/m$ to $P\bar{1}$ phase transitions on cooling to oxygen ordering. Local structural studies using neutron total scattering reveal that well-ordered GeO_5 square pyramidal groups form in the structure at low temperature, but that O_{int} becomes significantly more disordered in the high-conductivity, high-temperature structures, with a transition to more trigonal-bipyramid-like average geometry. We relate the higher conductivity of Bi materials to the presence of several O_{int} sites of similar energy in the structure, which correlates with its less-distorted low-temperature average structure.

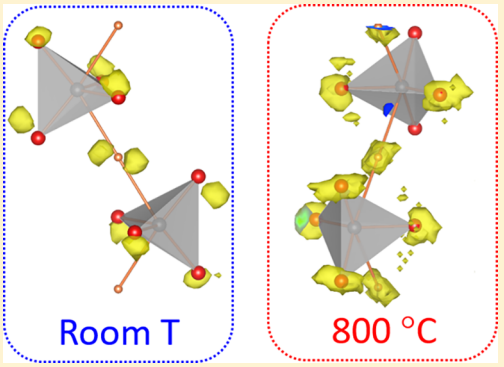

INTRODUCTION

Apatites are materials with the general formula $A_{10}(TO_4)_6X_{2\pm x}$, where A = alkaline or rare earth metal; M = Ge, Si, or P; and X = halides, O^{2-}, or $[OH]^-$. Compounds adopting this structure type are ubiquitous both as natural biomaterials and as synthetic functional materials with a range of technological applications. They are therefore of significant research interest in areas as diverse as materials chemistry, physics, engineering, medicine, archeology, and conservation science.

In all its roles, the fine details of the apatite structure, and in particular short-range local structure, have a critical impact on its physical or structural properties. For example, symmetry-lowering deviations from the ideal apatite structure and differing arrangements of ions in its channels are important to the function of natural bone and tooth enamel (carbonated calcium phosphate hydroxyapatite) and the use of apatite-type synthetic materials in bone grafts and implants.[1−5] In particular, the details of the local coordination environment of Ca^{2+} ions are necessary for understanding bone formation and diseases, but this information is hard to obtain given the experimental difficulty of techniques such as ^{43}Ca solid-state NMR.[6−8] Similar research questions regarding apatite-type materials are important in archeological science and anthropology.[9−12]

In the context of modern technological applications, departures from the ideal centrosymmetric crystal structures make some apatite-type materials second harmonic generation (SHG) active and potentially suitable for nonlinear optical (NLO) applications.[13,14] Apatite-type oxides are also promising hosts for the development of phosphors for solid-state lighting. In this application, the local environment and symmetry of the crystallographic sites occupied by the dopant activator ions significantly influence luminescence probabilities and energy transfer processes, and hence the emission properties of the phosphors.[15−18] Certain apatite-type lanthanum germanates and silicates also exhibit high oxide ion conductivities, making them applicable in oxygen sensors and pumps,[19] separation membranes,[20,21] and solid oxide fuel cells (SOFCs).[22−24] These applications are the focus of this paper.

The ideal apatite structure ($x = 0$ in $A_{10}(TO_4)_6X_{2\pm x}$) can be described as a framework in which columns of face-sharing AO_6 trigonal prisms share corners with TO_4 tetrahedra (dark green and gray polyhedra, respectively, in Figure 1a) to form channels running down the crystallographic *c*-axis; these channels are filled by A_6X_2 constituents (represented by light green and pink spheres in Figure 1a). The space group is usually hexagonal $P6_3/m$, although lower-symmetry variants are known.[25] The AO_6 trigonal prism twist angle ϕ has been used as a quantitative parameter indicative of the geometry of the framework and symmetry of the material.[26] If the size of the channels is large relative to the units occupying it, the A cations in the channels tend to be under-bonded and the tetrahedral T cations overbonded; to remove this unfavorable situation, the framework trigonal prisms twist. A recent density

Received: August 23, 2019
Published: October 16, 2019

DOI: 10.1021/acs.inorgchem.9b02544
Inorg. Chem. 2019, 58, 14853−14862

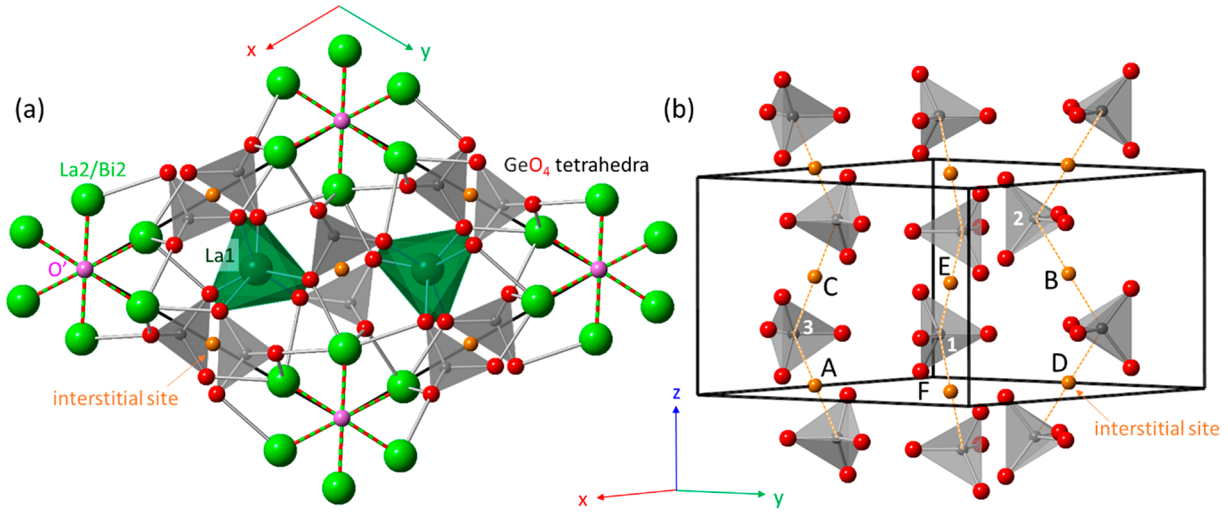

Figure 1. (a) Hexagonal $P6_3/m$ apatite structure, exemplified by the high-temperature average structure of $La_{10}(GeO_4)_6O_3$ viewed down the *c*-axis; (b) labels of different potential O_{int} sites (orange spheres, A−F) in the $P\bar{1}$ apatite structure. The gray tetrahedra show GeO_4 groups and are included to highlight their proximity to the O_{int}. Symmetry-unique GeO_4 tetrahedra are numbered.

functional theory (DFT) computational study[27] of a series of hexagonal and triclinic apatites with A cations of very similar sizes, $A_{10}(PO_4)_6F_2$ (A = Ca, Sr, Pb, Cd, Hg), found the symmetry lowering to be an electronic effect associated with mixing of the occupied $(n-1)d^{10}$ and the empty ns^0 states for A = Cd and Hg. In these cases the authors propose a particular displacive mode, associated with cooperative tilts of the TO_4 tetrahedra belonging to the $\Gamma_4^+\Gamma_6^+$ irreducible representation (irrep), as driving the $P6_3/m$ to $P\bar{1}$ phase transition.

Oxygen-excess (x = 1) $La_{10}(GeO_4)_6O_3$ and $La_8Bi_2(GeO_4)_6O_3$ are both excellent oxide ion conductors, with $\sigma \approx 7.8 \times 10^{-3}$ and 1.3×10^{-2} S/cm at 775 °C, respectively.[28] The room-temperature structure of $La_{10}(GeO_4)_6O_3$ has been described as triclinic from low-resolution powder neutron diffraction data,[29] whereas the high-temperature structure has not been reported. The structure of $La_8Bi_2(GeO_4)_6O_3$ has been studied by high-resolution synchrotron X-ray and neutron diffraction data and found to be triclinic at room temperature and hexagonal at 800 °C.[30] There is a general consensus in the literature, both from diffraction-based investigations of the average structure and from computational studies, that the most likely location for the extra oxygen (O_{int}) atoms in apatite-type germanates is between the opposite faces of adjacent GeO_4 tetrahedra (locations represented by orange spheres in Figure 1). In space group $P6_3/m$, these locations correspond to a single unique crystallographic site (Wyckoff site 6g). When the symmetry is lowered to triclinic $P\bar{1}$, however, they become six independent crystallographic sites. The potential locations of interstitial O_{int} sites in the unit cell are shown in Figure 1b and labeled A−F. Pramana et al.[29] located the O_{int} atoms on the B-sites of $La_{10}(GeO_4)_6O_3$, whereas Tate et al.[30] found the O_{int} atoms to be distributed over several sites of $La_8Bi_2(GeO_4)_6O_3$. The experimental limitations in these works were the reliance on difference Fourier maps generated from relatively low-resolution powder neutron diffraction data in the former case and the use of the HAADF-STEM method, which is an inherently two-dimensional probe, in the latter.

The aim of this work was to experimentally probe the local structure of two apatite-type oxide ion conductors, $La_{10}(GeO_4)_6O_3$ and $La_8Bi_2(GeO_4)_6O_3$, as a function of temperature and correlate the local structure with the measured properties and with density functional theory (DFT) simulations of their oxide ion conductivity. In addition to these triclinic examples, we also studied hexagonal $La_8Sr_2(GeO_4)_6O_2$ (x = 0, no interstitial oxygen) to provide a reference point for the interpretation of structure−property relationships in the two triclinic oxygen-excess materials. We used variable-temperature neutron total scattering and reverse Monte Carlo (RMC) modeling to derive local structural models that account for the higher conductivity found for $La_8Bi_2(GeO_4)_6O_3$.

EXPERIMENTAL SECTION

Synthesis. Two 5 g samples of $La_8R_2(GeO_4)_6O_{2+x}$ for each of R = Sr, La, and Bi were prepared by hand-grinding stoichiometric amounts of La_2O_3 (Acros, 99.9%, heated at 950 °C for 12 h prior to synthesis), $SrCO_3$ (Fisher, 99.9%), Bi_2O_3 (Fisher, 99.9%), and GeO_2 (Acros, 99.999%). The samples were heated at 1100 °C for 16−36 h followed by a further heating at 1300 and 1100 °C for R = Sr, La and R = Bi, respectively, with intermittent grinding. The two 5 g batches were mixed and then heated at 1300, 1200, and 1100 °C for R = Sr, La, and Bi, respectively. All products were pale cream in color. Samples were also heated at 1000 °C for 12 h immediately prior to neutron/synchrotron powder diffraction studies on HRPD and I11. For $La_8Bi_2(GeO_4)_6O_3$ this treatment appeared to give rise to small impurity phases, and a fresh 5 g sample was prepared for later neutron total scattering data collections on POLARIS. All heating and cooling rates were set to 10 °C min^{-1}. Phase purity was assessed using laboratory X-ray powder diffraction data collected on a D8 Bruker Advance with Cu $K\alpha_{1/2}$ radiation, a Ni filter and Lynxeye detector. Samples were mounted on Si zero-background slides and typically scanned over a $10° \leq 2\theta \leq 80°$ range in 0.02° steps for 1 s per step.

Synchrotron Powder Diffraction. Synchrotron X-ray powder diffraction data were collected using a wavelength of λ = 0.8259211 Å, determined from a Si standard, on samples loaded into 0.3 mm diameter fused silica capillaries at the Diamond Light Source beamline I11. A hot air blower was used to control the temperature for variable temperature data collections. The samples were heated from 30−800 °C in 25 °C steps with a scan time of 1 h at 30 and 800 °C and 5 min for the intervening scans. The temperature was calibrated with an Al_2O_3 standard. Room temperature experiments on $La_8Sr_2(GeO_4)_6O_2$ to investigate unusual peak shapes used 30 min data collections with λ = 0.824681 Å.

DOI: 10.1021/acs.inorgchem.9b02544
Inorg. Chem. 2019, 58, 14853−14862

Neutron Scattering. High-resolution neutron powder diffraction data were collected for $La_8R_2(GeO_4)_6O_{2+x}$ in 11 mm vanadium cans (sample heights of ∼2.5 cm and masses of ∼3.0 g) on the High Resolution Powder Diffraction (HRPD) instrument at the ISIS Neutron and Muon Source. A 6 h measurement was collected at room temperature for all samples. For $La_{10}(GeO_4)_6O_3$ 6 min measurements were recorded from 100−840 °C in 20 °C increments to follow cell parameter evolution, followed by six 1 h measurements at 850 °C. Equivalent data were recorded for $La_8Bi_2(GeO_4)_6O_3$ but with a maximum temperature of 800 °C. For $La_8Sr_2(GeO_4)_6O_2$, 6 min measurements were recorded from 90−850 °C. Data of suitable quality for PDF analysis were recorded using the ISIS POLARIS diffractometer on ∼2.7 g samples of $La_8R_2(GeO_4)_6O_{2+x}$ in 8 (R = La, Sr) or 6 (R = Bi) mm vanadium cans with sample heights of ∼4.7 cm. Six 1 h measurements were recorded for each sample at room temperature. Six 1 h measurements were performed at 850 °C for R = La and 800 °C for R = Bi.

Data were processed for Rietveld refinement using routines within Mantid software and an absorption correction was applied.[31] PDF data were processed using *GudrunN*[32] version 5 to produce $S(Q)$ data and the STOG[33] software package was used to create $G(r)$ and $F(Q)$ files. $G(r)$ data were produced using Q_{max} = 35 Å^{-1} and a Lorch function[34] was applied to remove Fourier ripples due to the limited Q_{max}. Low-r data were Fourier-filtered as follows: R = Sr, $r \leq 1.6$ Å (room temperature); R = La, $r \leq 1.52$ Å (room temperature) and $r \leq 1.55$ Å (850 °C); R = Bi, $r \leq 1.55$ Å (room temperature) and $r \leq 1.57$ Å (800 °C).

Rietveld Refinement. Rietveld refinements were performed using TOPAS v6.[35,36] Average structural models were derived from starting models published by Pramana et al. (R = La,[29] Sr[37]) and Tate et al. (R = Bi[30]). For combined refinements, HRPD bank 1 (2θ = 168.567°), bank 2 (2θ = 90.2481°), and synchrotron data were simultaneously fitted. Instrument calibration constants, wavelengths, and instrumental contributions to peak shapes were determined using Si or LaB_6 standards. Backgrounds were described using a 12th-order Chebyshev polynomial, and an additional broad pseudo-Voigt peak was used to describe scattering from the capillary. Peak shapes were described using conventional functions for these diffractometers, with a spherical harmonic function applied to describe *hkl*-dependent sample strain broadening.[38] When fitting multiple data sets, the same spherical harmonic function was used for each, with appropriate scaling onto each *x*-axis. An absorption correction was refined for X-ray data, and the value was consistent with that expected based on the capillary diameter and packing density. For analysis of rapid variable-temperature data sets used to extract unit cell parameters, the peak shapes, absorption corrections, and atomic coordinates were fixed at values derived from long data collections. Details of the refined structural parameters and agreement factors obtained are included in tables in the Supporting Information.

PDF Analysis. Total scattering analysis was performed using *TOPAS* v6[35,36] for small-box analysis by converting the $G(r)$ data produced by STOG into $D(r)$ normalized to the sum of the scattering of all atomic pairs according to standard formalisms.[39] RMCProfile[40] was used for big-box analysis. The $G(r)$ and $F(Q)$ produced by STOG and the Bragg scattering data from POLARIS bank 3 (2θ = 52.2461°) were used in the RMCProfile refinement. The $G(r)$ data were fitted as $D(r)$; 5 × 5 × 4 (∼50 × 50 × 30 Å; $\alpha \approx \beta \approx 90°$, $\gamma \approx 120°$) supercells were generated from the Rietveld models containing 4200 sites for R = Sr. For R = La, Bi, an extra 600 or 1200 sites were used to describe interstitial oxygen (O_{int}) positions A−F (Figure 1b), and equivalent vacancy positions. Site swapping procedures were used during the RMCProfile modeling to test data sensitivity to different O_{int} distributions. Minimum distance restraints were applied to prevent unreasonably short atomic approaches, and weak bond valence restraints were applied to maintain chemically plausible structures. Convergence and a good fit to experimental data was typically achieved after approximately 5 × 10^6 moves (approximately 15 h on a standard desktop PC). A minimum of 8 different configurations were used for each set of data fitted and the resulting configurations averaged during data analysis. "Cloud plot" figures were drawn using the VESTA software package.[41]

RESULTS AND DISCUSSION

Average Structure and Phase Transitions. Powder diffraction showed that high purity samples of $La_8R_2(GeO_4)_6O_{2+x}$ (R = Sr, La, Bi) could be prepared. In the large samples prepared for neutron scattering experiments, the R = Sr sample contained an $\lesssim$1 wt % Sr_2GeO_4 impurity, the R = La sample $a \lesssim$ 1% La_2GeO_5 impurity and the R = Bi sample a $\lesssim$ 1% $La_2Ge_2O_7$ impurity. Rietveld plots of combined synchrotron X-ray and HRPD neutron refinements are given in the Figure S1−S6 for room temperature (R = Sr, La, Bi) and 850/800 °C (R = La, Bi) data.

There has been some debate in the literature as to the true symmetry of the R = Sr (x = 0) phase; the presence of apparent peak splittings and broadening in the reported room temperature powder diffraction patterns prompted some authors to propose monoclinic symmetry at room temperature.[26] We also observed unusual peak splittings in samples synthesized at 1300 °C, but found that they could be explained by assuming that a mixture of hexagonal phases with slightly different cell parameters was present, suggesting compositional inhomogeneity. The fits obtained to high-resolution synchrotron X-ray diffraction data using a multiphase model in which cell parameters vary linearly with composition are shown in Figure S1. Heating to higher temperature (e.g., 1350 °C for 16 h) produced a phase with sharp peaks consistent with hexagonal $P6_3/m$ symmetry, as shown by the fits in Figure S2. We therefore conclude this is the correct space group for room-temperature R = Sr. Consistent with earlier studies, Rietveld refinement using both low- and high-temperature data suggested that Sr is located primarily (95%) on the A1 trigonal prismatic 4f site (dark green polyhedra in Figure 1).

Room-temperature powder patterns for R = La and Bi are significantly more complex, in line with the $P\bar{1}$ symmetry previously reported.[29,30] Samples showed a significant *hkl*-dependence to their peak shape, which is consistent with the strain broadening expected from the symmetry-lowering phase transition (discussed below) that occurs as they are cooled from high temperature. Peak shapes could be described by convoluting a *hkl*-dependent spherical harmonic function describing strain broadening onto the instrumental and isotropic sample contributions to the peak shape. We note that this approach is not possible in the RMCProfile modeling discussed below. Bi was found to occupy solely the A2 site within uncertainty.

One of the aims of this study is to identify the positions of the additional oxygen in R = La and Bi (x = 1 in $La_8R_2(GeO_4)_6O_{2+x}$) compared to Sr (x = 0); we call this 27th oxygen per formula unit O_{int}. The distribution of the excess oxygen atoms over likely sites A−F (Figure 1b) was determined by combined Rietveld fitting of synchrotron X-ray and HRPD high resolution neutron powder data. After refining a model with no O_{int}, oxygens were introduced on 2i Wyckoff sites close to positions A−F with occupancy 1/12 (giving one O_{int} per formula unit or x = 1). Their occupancies were refined with a soft restraint applied to maintain the overall O_{27} composition, a constrained minimum value of zero and a soft restraint was applied to keep them close to the midpoint of two tetrahedra (an inversion center in $P\bar{1}$). Repeated cycles of full Rietveld refinement and randomization of occupancies and coordinates consistently showed low or zero occupancy of sites

DOI: 10.1021/acs.inorgchem.9b02544
Inorg. Chem. 2019, 58, 14853−14862

Table 1. Important Structural Parameters

cell param.[a]	a (Å)	b (Å)	c (Å)	α (deg)	β (deg)	γ (deg)	V (Å^3)
Sr	9.90260(2)	9.90260(2)	7.32501(3)	90	90	120	622.067(3)
La	9.9412(1)	9.9190(1)	7.30337(6)	90.914(1)	88.1994(16)	120.8202(9)	618.15(1)
Bi	9.9042(1)	9.89656(1)	7.34419(7)	90.568(1)	89.174(7)	120.172(1)	622.27(1)
site occ.	A	B	C	D	E	F	
Sr	0	0	0	0	0	0	
La	0.08(1)	0.46(1)	0	0	0	0	
Bi	0.22(1)	0.23(1)	0.06(1)	0	0	0	

quantity	$\delta(a,b)$ (%)[b]	δ (ang, °)[b]	α_V ($\times 10^{-6}$ K^{-1})[c]	twist (ϕ,°)	Ge−O (Å)[d]	Tet angles[e]	RMC tet fwhm[f]
Sr	0	0	26.5(2)	23	1.741	103.8−114.9 (3.7)	20.3
La	0.11	3.54	29.1(6)	19−27 = 23(5)	1.777	91.8−136.6 (10.4)	23.2
Bi	0.04	1.56	29.0(5)	18−27 = 22(3)	1.765	90.8−128.9 (9.3)	30.2

[a]Room-temperature values. [b]Unit-cell distortions as % difference of a and b from their average and sum of angle differences from 90/120°. [c]Volume coefficient of thermal expansion quoted from 100 to 700 °C. [d]Room-temperature average Ge−O bond length from Rietveld refinements. [e]Room-temperature range of tetrahedral bond angles with standard deviation of values in parentheses. [f]fwhm extracted by fitting a Gaussian curve to the range of tetrahedral bond angles in RMCProfile configurations.

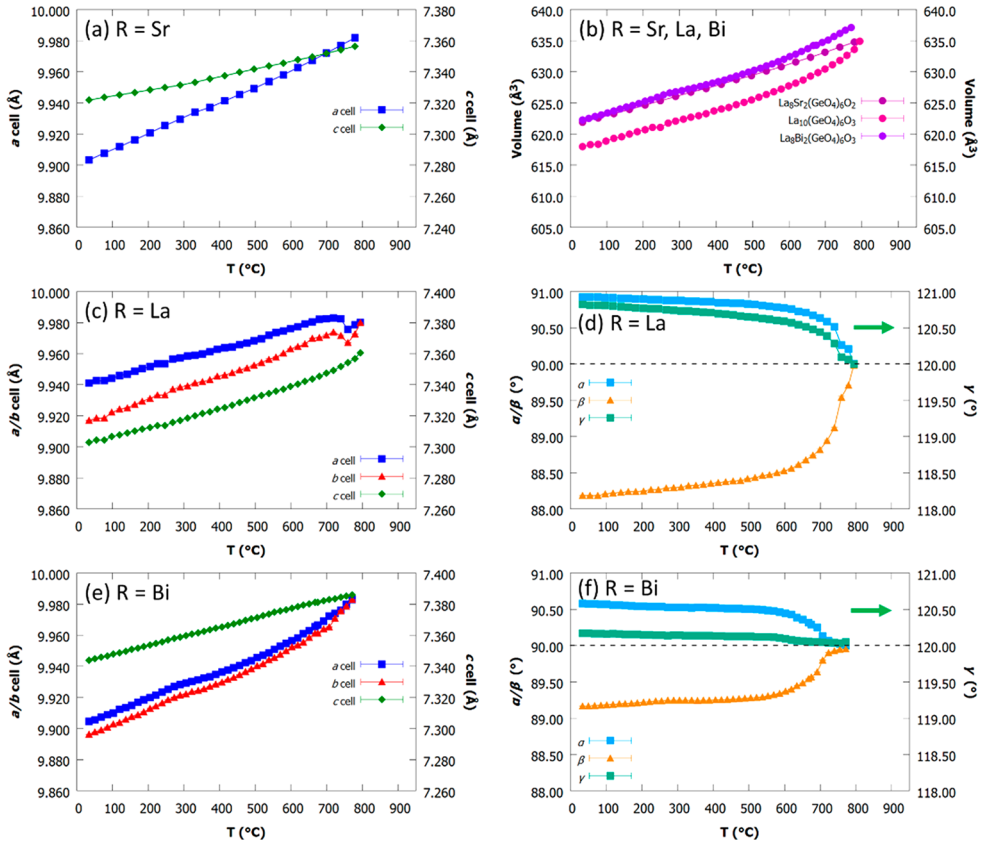

Figure 2. Unit-cell edges and angles derived from variable-temperature synchrotron powder diffraction studies of $La_8R_2(GeO_4)_6O_{2+x}$. (a) R = Sr; (b) volume of all phases; (c, d) R = La; (e, f) R = Bi. For R = La, Bi, a triclinic model was used at all temperatures. Note that γ ($\approx$ 120°) is plotted on the right-hand scale of d and f to emphasize the cell-angle convergence at the phase transition to $P6_3/m$.

D, E, and F. Final O_{int} occupancies at sites near A/B/C were 0.08(1)/0.46(1)/0.00(1) corresponding to a total O content of 27.08(4) for R = La, and 0.22(1)/0.23(1)/0.06(1) total = 27.00(6) for R = Bi. Removing restraints on the O_{int} occupancy gave a total oxygen content per cell of 27.19(5) and 27.02(6) for R = La and Bi, respectively. Because the change in fit quality was minimal in these free refinements (e.g., R_{wp} 4.146 to 4.141%.), and given the correlation between oxygen occupancies and other parameters, we choose to report models soft-restrained to an overall O_{27} composition. Performing equivalent analysis using lower resolution but higher signal-to-noise POLARIS data for R = La gave essentially identical occupancies of 0.06(1)/0.43(1)/0.00(1) for A/B/C sites. For R = Bi, POLARIS data were recorded on a physically different sample and gave A/B/C/D/E/F occupancies of 0.13(1)/0.21(1)/0.13(1)/0.00(1)/0.02(1)/0.01(1). These differences could reflect the difficulties in determining oxygen content by Rietveld refinement, as discussed below, or minor changes in oxygen distribution due to different sample thermal histories.

Even using neutrons, the contribution of the single O_{int} per unit cell to the total scattering is relatively small (2.5%), such that the determination of O_{int} positions is challenging from

DOI: 10.1021/acs.inorgchem.9b02544
Inorg. Chem. 2019, 58, 14853−14862

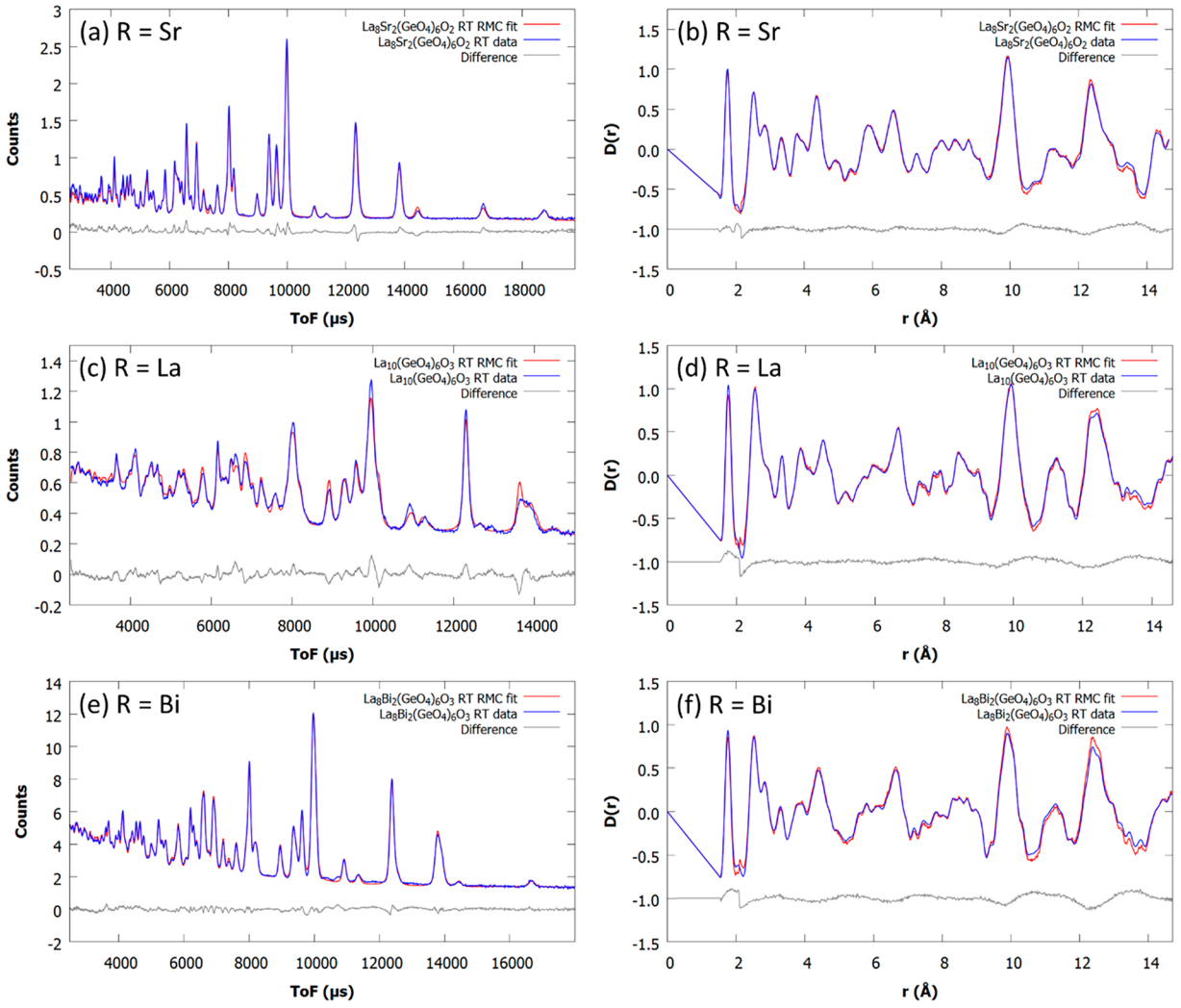

Figure 3. Representative RMCProfile fits at room temperature of $La_8R_2(GeO_4)_6O_{2+x}$: (a) R = Sr Bragg, (b) R = Sr PDF, (c) R = La Bragg, (d) R = La PDF, (e) R = Bi Bragg, (f) R = Bi PDF.

powder diffraction data. It is also worth noting that the symmetry reduction from $P6_3/m$ to $P\bar{1}$ could give rise to six different domains in a single-crystal based on the different basis vector choices relative to the parent structure. For a polycrystalline sample, this means there are six equivalent cell parameter choices with similar but subtly different values. These are tabulated for R = La in Table S6. Choosing a different set of cell parameters in the triclinic fit is equivalent to selecting a different domain, and will change the labeling of the various O_{int} sites (Table S6). Care must therefore be taken when comparing different refined models. Despite these caveats, our data suggest the B site has significant occupancy in both the La and Bi phase, with some density on site A. Ge sites Ge2 and Ge3, which lie on the BD and AC O_{int} chains respectively, show the most significant departure from tetrahedral bond angles, consistent with this occupation pattern. In contrast, tetrahedral bond angles in Ge1, which lie along the EF chains, remain relatively undistorted with standard deviations of the six tetrahedral angles similar to those in the hexagonal R = Sr case. Average $Ge1O_4$ bond angles and standard deviations of 109.4/4.6, 109.2/5.4, and 109.6/3.7° were obtained for R = La, Bi, and Sr, respectively. Values for all tetrahedra are given with other important structural parameters for the three phases in Table 1.

Figure 2 shows the unit-cell parameter evolution for each sample between room temperature and ~850 °C extracted by Rietveld refinement using synchrotron X-ray data. Values obtained from high-resolution neutron powder diffraction experiments are essentially identical and are shown in Figure S7. Each material shows positive thermal expansion with α_{Vol} = 26.5(2), 29.1(6), and 29.0(5) × 10^{-6} K^{-1} between 100 and 700 °C for R = Sr, La, and Bi respectively. For R = La and Bi, we see a clear indication of a phase transition to hexagonal symmetry at T = 780 and 740 °C with a and b cell edges converging, angles α/β approaching 90°, and angle γ approaching 120°. Although a symmetry analysis using ISODISTORT[42] shows that a $P6_3/m$ to $P\bar{1}$ transformation could occur via a number of intermediate subgroups (e.g., $P\bar{3}$, $P2_1/m$), it can be described using a single $\Gamma_4^+\Gamma_6^+$ irrep describing O_{int} ordering, and is allowed to be continuous by Landau theory. We see no evidence in the diffraction data for simple intermediate phases, which would all require at least one 90° cell angle. We do see a subtle change in thermal expansion for R = Bi in the X-ray and neutron data around 250 °C, which could suggest the onset of partial O mobility. One notable feature in Figure 2 and Table 1 is the smaller metric distortion from hexagonal for R = Bi than R = La, manifested in the smaller differences between the unit cell parameters a and b,

DOI: 10.1021/acs.inorgchem.9b02544
Inorg. Chem. 2019, 58, 14853−14862

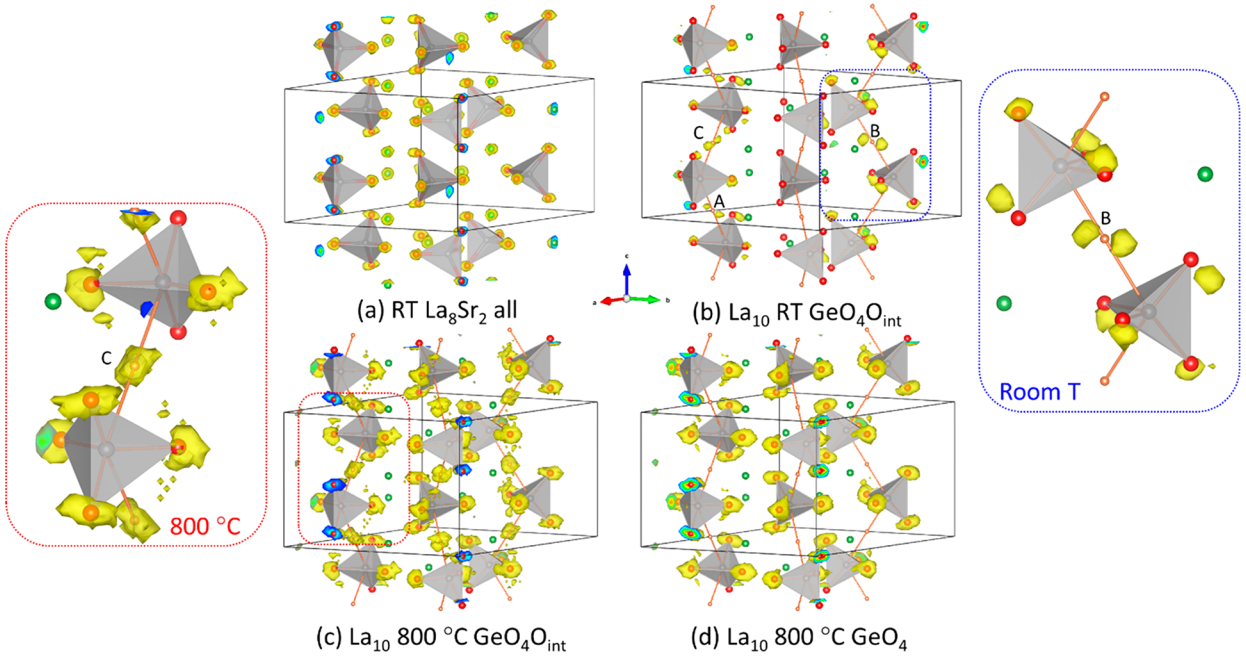

Figure 4. Cloud plots showing volumes enclosing oxygen sites in (a) $La_8Sr_2(GeO_4)_6O_2$ and (b–d) $La_{10}(GeO_4)_6O_3$. (a) Clouds for all atoms. (b) Only GeO_5 groups where O_{int} is part of Ge coordination sphere at room temperature. (c) Only GeO_5 groups at 800 °C. (d) Only GeO_4 groups at 800 °C. Small orange spheres show ideal O_{int} sites and green spheres A sites. Tetrahedra show GeO_4 groups in the high-temperature $P6_3/m$ structure. In b, the displacement of clouds from tetrahedral positions shows the local distortion of GeO_5 groups. The yellow surface is drawn at 2% of the maximum grid value in each plot; contours of blue to red where cloud surfaces intersect the cell edges show the population probability of different regions.

and the smaller deviations of the unit-cell angles from 90 and 120° for R = Bi; we return to this point below.

As discussed in the Introduction, previous workers have described the $P6_3/m$ to $P\bar{1}$ phase transition in Cd and Hg fluoro-phosphate O_{int}-free apatites in terms of a soft mode $\Gamma_4^+\Gamma_6^+$ irrep distortion, which causes a cooperative tilting of tetrahedra when frozen into the structure. Instead of using conventional crystallographic fractional coordinates, we can describe our room temperature structures of the $P\bar{1}$ La phase in terms of the high-temperature $P6_3/m$ parent structure plus the amplitude of 63 symmetry-adapted-distortion-modes using the language of Campbell, Stokes, and co-workers.[42] We find that 16 of the 63 allowed modes have irrep $\Gamma_4^+\Gamma_6^+$. These $\Gamma_4^+\Gamma_6^+$ modes appear to dominate the structural distortion, with 6 of the 9 largest amplitude modes belonging to this irrep. These modes alone describe the essence of the GeO_4 displacements and distortions. We see similar behavior for R = Bi, and histograms of mode amplitudes are included for both phases in Figure S8. Comparing mode amplitudes between R = La and R = Bi, we see, as expected, that the two structures display very similar distortions. On average, mode amplitudes (which give the root-summed-squared displacement of atoms in the child cell) for R = Bi are around 2/3 of their values for R = La, another representation of its lower distortion. The most significant difference between the two structures is in the O4 (O′) z-coordinate. O4 is coordinated exclusively by A2 cations and its position could be influenced by the lone pair cations on these sites, as indicated in previous theoretical studies.[43]

Local Structure. Further insight into the coordination environments of O_{int}, their influence on the surrounding coordination polyhedra, and the implication of their temperature evolution on conductivity requires a local rather than average structural probe. We have used big-box modeling using 5 × 5 × 4 supercells within the RCMProfile package to simultaneously fit Bragg, $D(r)$ and $F(q)$ data from each sample.

For R = Sr excellent agreement with experimental data was obtained from each of 8 different RMCProfile starting configurations. Representative fits to Bragg and PDF data are shown in Figure 3a, b ($F(Q)$ fits shown in Figure S9). As expected for an ordered structure, the "cloud plots" of atomic density produced by folding the supercell configurations back into a single unit cell show good agreement with the average structural model (Figure 4a) and with the size of the atomic displacement parameters. Bond lengths and bond angle distributions around GeO_4 were as expected for regular tetrahedra. Fitting the observed distributions (Figure S10a, b) in all 8 configurations to Gaussian functions gave a mean Ge–O bond length of 1.7584(7) Å and O–Ge–O angles of 108.91(3)°; the full width at half-maximum (fwhm) of the distributions were 0.176(1) Å and 20.33(7)° respectively. The corresponding bond length determined from Rietveld refinement was 1.741(8) Å and angles ranged from 103.9 to 114.9°. The difference between the Rietveld- and RMCProfile-derived bond lengths is presumably caused by the well-known shortening of refined bond lengths when harmonic displacement parameters are used for groups undergoing correlated motion.[44]

For R = La and Bi, four models were tested to describe the O_{int} distribution and how it influences conclusions about local structure. These involved starting O_{int} atoms on sites to mimic the distribution indicated by Rietveld refinement, or statistically placing them across all available sites. During RMCProfile modeling O_{int} was then either limited to swapping between just the Rietveld sites or allowed to visit all sites A–F. After convergence we find that the O_{int} distribution broadly follows that derived by Rietveld refinement (Table S7). This occurs

DOI: 10.1021/acs.inorgchem.9b02544
Inorg. Chem. 2019, 58, 14853–14862

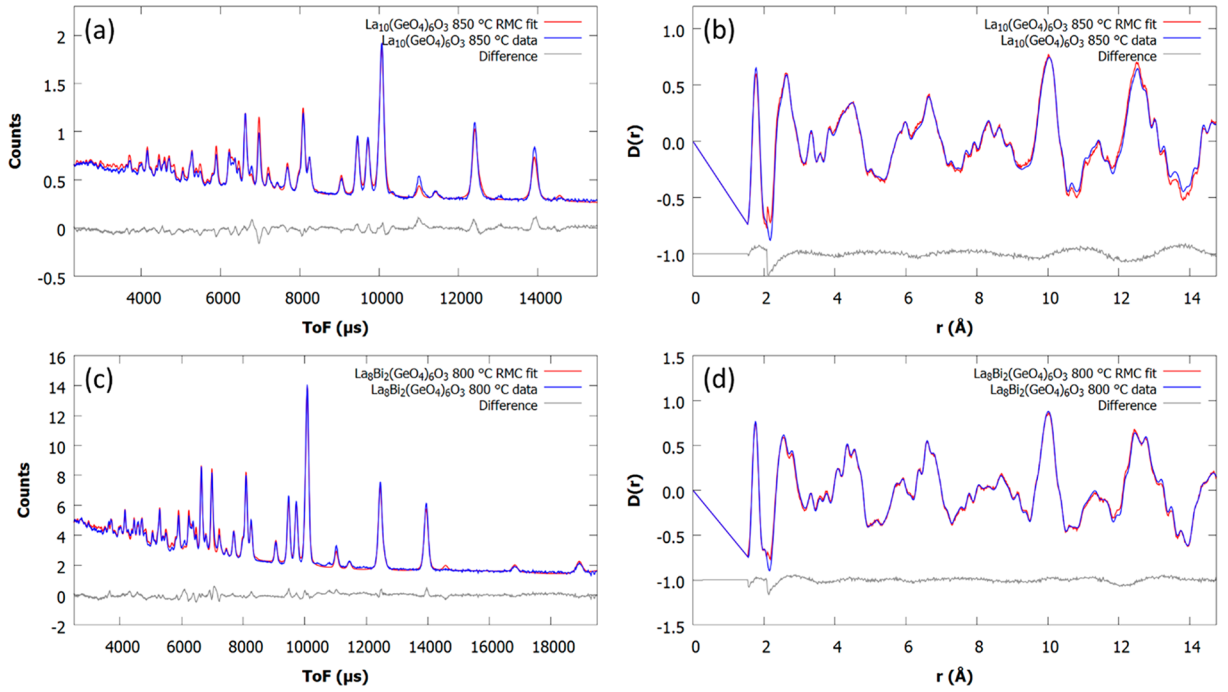

Figure 5. Representative RMCProfile fits of $La_8R_2(GeO_4)_6O_3$ at 850 °C (R = La) and 800 °C (R = Bi); (a) R = La Bragg, (b) R = La PDF, (c) R = Bi Bragg, and (d) R = Bi PDF.

despite RMC methods favoring random models and is caused, at least in part, by the GeO_4 distortions present in the Rietveld-derived average model, meaning that certain O_{int} sites provide more favorable local environments in terms of an absence of short contacts with neighboring oxygens. Importantly, analysis of different models showed that the local structural information derived and discussed below was independent of the O_{int} model used. The results discussed are therefore based on the average of eight starting configurations in which O_{int} was allowed to populate all possible sites starting from a statistical distribution.

Figure 3 shows typical fits to the room-temperature Bragg and $D(r)$ data for R = La (Figure 3c, 3d) and R = Bi (Figure 3e, 3f); Figure 5 shows equivalent fits above the $P\bar{1}$ to $P6_3/m$ transition. $F(Q)$ plots are included in Figure S9. We see good agreement between observed and calculated data in all cases. The largest discrepancies are the reflections for R = La at ~13 500 μs ($d \approx 4$ Å) which derive from the parent (2, −1, 1): although the overall intensity of this reflection is captured correctly, we are not able to describe the *hkl*-dependent peak shape during RMCProfile modeling. We note that this peak is fitted much better in the Rietveld plot of Figure S3d. Because the overall intensity is modeled correctly, this will not influence our conclusions on local structure.

The most important information from PDF modeling concerns the local coordination geometry around O_{int} and how it changes with temperature. By analyzing each Ge site in the big-box configuration, we can probe individual GeO_n groups and how they vary depending on the location of O_{int}. Histograms of bond distances and angles around Ge (Figure S10) show that the GeO_n polyhedra fall into two distinct categories: GeO_4 tetrahedra (84% of total) that are remote from O_{int} sites and GeO_5 polyhedra (16%) wherein O_{int} enters the coordination sphere. This is consistent with ^{17}O NMR studies on $La_8Y_2Ge_6O_{27}$.[45] Although it would be possible to produce GeO_6 groups if two nearby O_{int} sites were simultaneously occupied and close to the same Ge (e.g., B and D close to Ge2 in Figure 1b), the number of such groups is extremely small in our configurations. We can produce cloud plots showing the local geometries near O_{int} by folding all the GeO_4O_{int} groups from all configurations back into a single crystallographic cell as shown in Figure 4b, c for R = La. Because the plots of Figure 4 use a single unit cell, they average the big-box configuration in a fashion similar to the average crystallographic model meaning that the "double clouds" or "peanut" O_{int} shapes represent sites that are not occupied simultaneously. We can see, however, that O_{int} sites are relatively localized at low temperature (Figure 4b) but become significantly more diffuse at high temperature (Figure 4c).

The cloud plots of Figure 4 help understand the origin of the high oxide ion conductivity in oxygen excess apatite-type germanates. Recent density functional theory (DFT) studies of the $La_{10-y}Bi_yGe_6O_{27}$ (y = 0, 2, 4) series, supported by neutron scattering experiments, have calculated the oxide ion migration pathways in these materials and provided new insight into the lone pair effects associated with the presence of Bi(III).[43,46] The ab initio simulations identified four oxide ion exchange mechanisms contributing to the ionic conductivity, with the main one based on oxide ion transport in the *c*-direction via the $\cdots GeO_4 - GeO_5 - GeO_4 \cdots$ network. This mechanism, prevalent at all simulation temperatures for all compositions in the series, gives rise to ionic displacement clouds that are very similar in appearance to the atomic density map shown in Figure 4c.

Focusing on the geometries of individual GeO_n polyhedra, we find that GeO_4 tetrahedra are only slightly more distorted than in the R = Sr case (fwhm of angle distribution 20.3, 23.2, and 30.2° for R = Sr, La, and Bi, respectively), whereas the GeO_5 groups display a much broader distribution of bond angles with maxima at ~90, 140, and 160°. Bond-angle histograms are given in Figure S10. We can gain more insight into the geometry of the GeO_5 polyhedra from the histograms

DOI: 10.1021/acs.inorgchem.9b02544
Inorg. Chem. 2019, 58, 14853−14862

of Figures 6 and 7. Figure 6 shows a histogram of the difference-in-distance between O_{int} and its two neighboring Ge

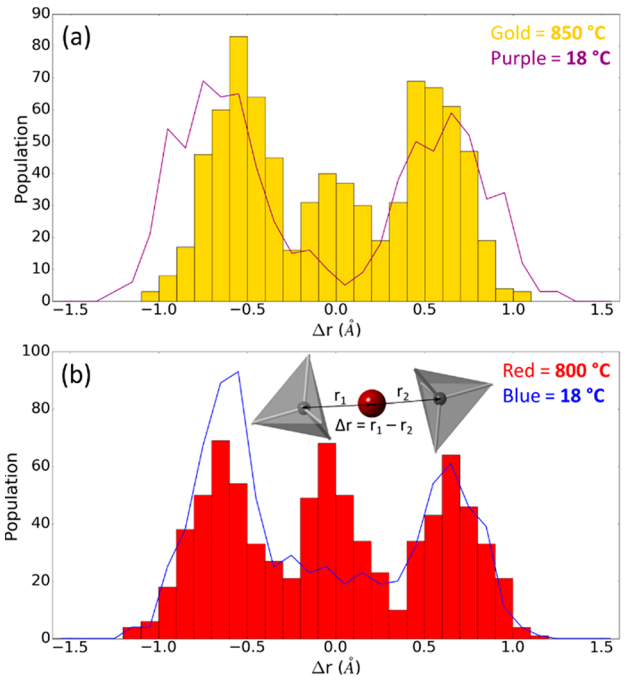

Figure 6. Histograms of ΔGe−O_{int} distances in (a) $La_{10}(GeO_4)_6O_3$ at room-temperature (purple line) and 850 °C (gold bars) and; (b) $La_8Bi_2(GeO_4)_6O_3$ at room-temperature (blue) and 800 °C (red). Distances Δr defined in inset to (b).

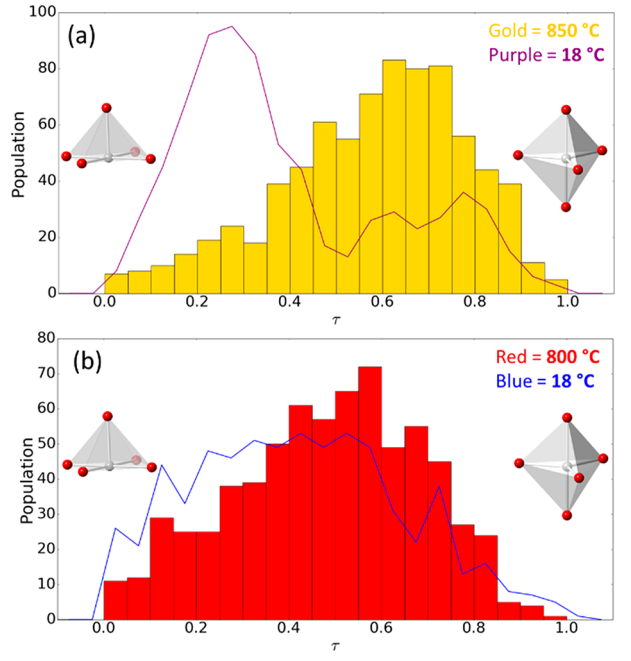

Figure 7. Histogram of τ values found in (a) $La_{10}(GeO_4)_6O_3$ at room temperature (purple line) and 850 °C (gold bars); (b) $La_8Bi_2(GeO_4)_6O_3$ at room temperature (blue line) and 800 °C (red bars).

(i.e., the Ge−O···Ge local asymmetry). For both R = La and R = Bi, we observe a strong preference for each O_{int} to have one short and one long Ge−O distance at room temperature. This is consistent with local bond-valence considerations. If we take a typical Ge−Ge separation of 4 Å, an O placed midway between the two would have a bond valence sum of ~1.0. Displacing O_{int} locally to give bond lengths of 1.6 and 2.4 (Δr = 0.8 Å as observed experimentally, Figure 6a) gives a more reasonable bond valence sum of ~1.7.

On heating above the $T_c \approx 750$ °C phase transition we see a marked change in the Δr histograms. The sharp peaks at $\Delta r = \pm 0.8$ Å move to slightly smaller values and we see a significant increase in the number of O_{int} located symmetrically between the two GeO_4 tetrahedra ($\Delta r \approx 0$). These can be viewed as Ge_2O_9 units as opposed to GeO_5 + GeO_4. Using $|\Delta r| \leq 0.25$ Å as a cut off (based on the shape of the Figure 6 histograms), we can quantify the % of O_{int} in Ge_2O_9 groups at room/high temperature as 6(2)/20(2) % and 15(3)/29(5) % for R = La and Bi respectively.

We can also probe the local coordination geometry of each GeO_5 group using the τ_5 parameter discussed by Addison and co-workers and defined as $\frac{\beta - \alpha}{60°}$, where β and α are the largest and second largest bond angles respectively.[47] τ_5 varies from 0 for a square pyramidal site to 1 for a trigonal bipyramid. Figure 7a, b superimpose low- and high-temperature τ_5 histograms for R = La and R = Bi. In the low-temperature $P\bar{1}$ structure we see that the GeO_5 groups are predominantly square planar in nature, whereas there is a shift in the distribution to predominantly trigonal bipyramidal at high temperature.

CONCLUSIONS

Our studies have provided important new insight into the structural properties of $La_8R_2(GeO_4)_6O_{2+x}$ phases and how these influence conductivity. For the low-conductivity, $x = 0$, O_{int}-free R = Sr phase, we find that it adopts the simple $P6_3/m$ structure at all temperatures. Apparent peak splittings in the powder diffraction patterns of samples prepared at 1300 °C or lower reflect compositional inhomogeneities. RMCProfile modeling of its local structure provides a benchmark for the other O_{int}-containing higher conductivity materials.

$La_{10}(GeO_4)_6O_3$ and $La_8Bi_2(GeO_4)_6O_3$ both adopt triclinic $P\bar{1}$ symmetry at room temperature and hexagonal $P6_3/m$ symmetry at high temperature, as previously reported. Rietveld refinement shows that the single O_{int} atom per formula unit lies between GeO_4 tetrahedra. Multiple sites can be occupied: the B site is strongly favored in $La_{10}(GeO_4)_6O_3$ and the A, B and C sites are occupied in $La_8Bi_2(GeO_4)_6O_3$. The preferential occupation of certain sites drives the phase transition to $P\bar{1}$. The less-complete site ordering for R = Bi presumably occurs due to the distribution of La and Bi atoms on the A2 site (2:1 on average, but there will be local deviations from this) leading to a range of energies for nearby O_{int} sites. Previous computational studies have also shown that the Bi lone pair gives rise to significant local structural distortions. Because of the similar neutron scattering lengths of La and Bi, our local studies cannot probe this aspect of the structure. The wider O_{int} distribution for R = Bi is presumably the reason why it shows a smaller distortion from hexagonal symmetry at room temperature than R = La. The presence of similar-energy O_{int} sites can then explain the lower phase transition temperature to $P6_3/m$ and underpin the higher O^{2-} conductivity of R = Bi. Less-stable O_{int} sites may also redistribute at low temperature, leading to the small discontinuity in the cell parameters observed at around 250 °C.

Local structural analysis shows that the O_{int} atoms are predominantly present in GeO_5 square planar units at room

DOI: 10.1021/acs.inorgchem.9b02544
Inorg. Chem. 2019, 58, 14853−14862

temperature, rather than in more symmetrical Ge_2O_9 units. At high temperature, the GeO_5 polyhedra adopt a more trigonal bipyramid character, and there is an increase in the number of units that can be classified as Ge_2O_9. This shows that, although the high-temperature structure retains significant aspects of the low-temperature structure, the phase transition leads to increased disorder of the O_{int} oxygens. The less-distorted R = Bi material also appears to have a higher proportion of Ge_2O_9-like groups at low temperature than R = La. This is again correlated to the higher O_{int} disorder caused by a range of local environments.

Previous computational studies have suggested that the most common conduction pathway in $La_{10}(GeO_4)_6O_3$ occurs through an interstitialcy mechanism that involves movement of O^{2-} along the *c*-axis between GeO_4 units via normal-site O^{2-} and O_{int}. Our experimental local structure analysis results are consistent with this hypothesis and suggest a distribution of sites is present between the GeO_4 tetrahedra at high temperature. Our static local structure snapshots hence sample the dynamic distribution of atoms that are present in the highly conducting phases.

In summary, total scattering studies have provided important insight into the local structure rearrangements that occur to accommodate the oxygen interstitial in $La_{10}(GeO_4)_6O_3$ and $La_8Bi_2(GeO_4)_6O_3$, and how these structures rearrange and become more disordered in the oxygen-conducting high-temperature phase.

■ ASSOCIATED CONTENT

Supporting Information

The Supporting Information is available free of charge on the ACS Publications website at DOI: 10.1021/acs.inorgchem.9b02544.

All Rietveld plots discussed in the text; plots of unit-cell parameters against temperature for all phases derived from neutron diffraction data; histograms of mode amplitudes and resulting atomic displacements; fits to neutron $F(Q)$ data; histograms of bond lengths and angles at low and high temperature from RMCProfile models; Rietveld-derived fractional coordinates; O_{int} distributions from RMCProfile models (PDF)

■ AUTHOR INFORMATION

Corresponding Authors

*Email: john.evans@durham.ac.uk.
*Email: ivana.radosavljevic@durham.ac.uk.

ORCID

Ivana Radosavljevic Evans: 0000-0002-0325-7229
John S. O. Evans: 0000-0001-6305-6341

Notes

The authors declare no competing financial interest.

■ ACKNOWLEDGMENTS

M.S.C. thanks Diamond Light Source and Durham University for a PhD studentship. I.R.E. acknowledges the Royal Society and the Leverhulme Trust for the award of a Senior Research Fellowship (SRF\R1\180040). We gratefully acknowledge the Science and Technology Facilities Council (STFC) for access to neutron beamtime at POLARIS (RB1610105) and HRPD (RB1610106), ISIS, and thank Dr. Helen Playford for assistance during data collection. We acknowledge Diamond Light Source for time on Beamline I11 under Proposal EE14188 and thank Dr. Claire Murray and Dr. Annabelle Baker for assistance during data collection.

■ REFERENCES

(1) Von Euw, S.; Wang, Y.; Laurent, G.; Drouet, C.; Babonneau, F.; Nassif, N.; Azais, T. Bone mineral: new insights into its chemical composition. *Sci. Rep.* **2019**, *9*, 8456.

(2) Fernandez de Grado, G.; Keller, L.; Idoux-Gillet, Y.; Wagner, Q.; Musset, A.-M.; Benkirane-Jessel, N.; Bornert, F.; Offner, D. Bone substitutes: a review of their characteristics, clinical use, and perspectives for large bone defects management. *J. Tissue Eng.* **2018**, *9*, 204173141877681.

(3) Pastero, L.; Bruno, M.; Aquilano, D. About the Genetic Mechanisms of Apatites: A Survey on the Methodological Approaches. *Minerals* **2017**, *7* (8), 139.

(4) Uskokovic, V. The role of hydroxyl channel in defining selected physicochemical peculiarities exhibited by hydroxyapatite. *RSC Adv.* **2015**, *5* (46), 36614−36633.

(5) Ma, G. B.; Liu, X. Y. Hydroxyapatite: Hexagonal or Monoclinic? *Cryst. Growth Des.* **2009**, *9* (7), 2991−2994.

(6) Laurencin, D.; Wong, A.; Dupree, R.; Smith, M. E. Natural abundance Ca-43 solid-state NMR characterisation of hydroxyapatite: identification of the two calcium sites. *Magn. Reson. Chem.* **2008**, *46* (4), 347−350.

(7) Lee, D.; Leroy, C.; Crevant, C.; Bonhomme-Coury, L.; Babonneau, F.; Laurencin, D.; Bonhomme, C.; De Paepe, G. Interfacial Ca^{2+} environments in nanocrystalline apatites revealed by dynamic nuclear polarization enhanced Ca-43 NMR spectroscopy. *Nat. Commun.* **2017**, *8*, 14104.

(8) Xu, J. D.; Zhu, P. Z.; Gan, Z. H.; Sahar, N.; Tecklenburg, M.; Morris, M. D.; Kohn, D. H.; Ramamoorthy, A. Natural-Abundance Ca-43 Solid-State NMR Spectroscopy of Bone. *J. Am. Chem. Soc.* **2010**, *132* (33), 11504−11509.

(9) Mamede, A. P.; Vassalo, A. R.; Piga, G.; Cunha, E.; Parker, S. F.; Marques, M. P. M.; Batista de Carvalho, L. A. E.; Goncalves, D. Potential of bioapatite hydroxyls for research on archeological burned bone. *Anal. Chem.* **2018**, *90* (19), 11556−11563.

(10) Piga, G.; Baro, M. D.; Escobal, I. G.; Goncalves, D.; Makhoul, C.; Amarante, A.; Malgosa, A.; Enzo, S.; Garroni, S. A structural approach in the study of bones: fossil and burnt bones at nanosize scale. *Appl. Phys. A: Mater. Sci. Process.* **2016**, *122* (12), 1031.

(11) Piga, G.; Santos-Cubedo, A.; Moya Sola, S.; Brunetti, A.; Malgosa, A.; Enzo, S. An X-ray Diffraction (XRD) and X-ray Fluorescence (XRF) investigation in human and animal fossil bones from Holocene to Middle Triassic. *Journal of Archaeological Science* **2009**, *36* (9), 1857−1868.

(12) Richards, M. P.; Schulting, R. J.; Hedges, R. E. M. Sharp shift in diet at onset of Neolithic. *Nature* **2003**, *425* (6956), 366−366.

(13) Evans, J. S. O.; Huang, J.; Sleight, A. W. Synthesis and structure of $ACa_9(VO_4)_7$ compounds, A = Bi or a rare earth. *J. Solid State Chem.* **2001**, *157* (2), 255−260.

(14) Jing, Q.; Dong, X. Y.; Yang, Z. H.; Pan, S. L.; Zhang, B. B.; Huang, X. C.; Chen, M. W. The interaction between cations and anionic groups inducing SHG enhancement in a series of apatite-like crystals: A first-principles study. *J. Solid State Chem.* **2014**, *219*, 138−142.

(15) Huang, C. H.; Chen, T. M. A Novel Single-Composition Trichromatic White-Light $Ca_3Y(GaO)_3(BO_3)_4$: Ce^{3+},Mn^{2+},Tb^{3+} Phosphor for UV-Light Emitting Diodes. *J. Phys. Chem. C* **2011**, *115* (5), 2349−2355.

(16) Liu, H. K.; Luo, Y.; Mao, Z. Y.; Liao, L. B.; Xia, Z. G. A novel single-composition trichromatic white-emitting $Sr_{3.5}Y_{6.5}O_2(PO_4)_{1.5}(SiO_4)_{4.5}$: $Ce^{3+}/Tb^{3+}/Mn^{2+}$ phosphor: synthesis, luminescent properties and applications for white LEDs. *J. Mater. Chem. C* **2014**, *2* (9), 1619−1627.

(17) Mei, L. F.; Liu, H. K.; Liao, L. B.; Zhang, Y. Y.; Kumar, R. V. Structure and photoluminescence properties of red-emitting apatite-

DOI: 10.1021/acs.inorgchem.9b02544
Inorg. Chem. 2019, 58, 14853−14862

type phosphor $NaY_9(SiO_4)_6O_2:Sm^{3+}$ with excellent quantum efficiency and thermal stability for solid-state lighting. *Sci. Rep.* **2017**, *7*, 15171.
(18) Rodriguez-Garcia, M. M.; Williams, J. A. G.; Evans, I. R. Single-phase white-emitting phosphors based on apatite-type gadolinium silicate, $Gd_{9.33}(SiO_4)_6O_2$ doped with Dy^{3+}, Eu^{3+} and Tb^{3+}. *J. Mater. Chem. C* **2019**, *7* (25), 7779−7787.
(19) Yuan, D.; Kröger, F. A. Stabilized Zirconia as an Oxygen Pump. *J. Electrochem. Soc.* **1969**, *116* (5), 594−600.
(20) Sunarso, J.; Baumann, S.; Serra, J. M.; Meulenberg, W. A.; Liu, S.; Lin, Y. S.; Diniz da Costa, J. C. Mixed ionic−electronic conducting (MIEC) ceramic-based membranes for oxygen separation. *J. Membr. Sci.* **2008**, *320* (1−2), 13−41.
(21) Dyer, P. N.; Richards, R. E.; Russek, S. L.; Taylor, D. M. Ion transport membrane technology for oxygen separation and syngas production. *Solid State Ionics* **2000**, *134* (1−2), 21−33.
(22) Wachsman, E. D.; Duncan, K. L. *Ceria/Bismuth Oxide Bilayered Electrolytes for Low Temperature Solid Oxide Fuel Cells*; Electrochemical Society Inc: Pennington, NJ, 1999; Vol. *99*, p 264−274.
(23) Skinner, S. J.; Kilner, J. A. Oxygen ion conductors. *Mater. Today* **2003**, *6* (3), 30−37.
(24) Brett, D. J. L.; Atkinson, A.; Brandon, N. P.; Skinner, S. J. Intermediate temperature solid oxide fuel cells. *Chem. Soc. Rev.* **2008**, *37* (8), 1568−1578.
(25) White, T. J.; Dong, Z. Structural derivation and crystal chemistry of apatites. *Acta Crystallogr., Sect. B: Struct. Sci.* **2003**, *59* (1), 1−16.
(26) Pramana, S. S.; White, T. J.; Schreyer, M. K.; Ferraris, C.; Slater, P. R.; Orera, A.; Bastow, T. J.; Mangold, S.; Doyle, S.; Liu, T.; Fajar, A.; Srinivasan, M.; Baikie, T. Pseudomorphic 2A -> 2M -> 2H phase transitions in lanthanum strontium germanate electrolyte apatites. *Dalton Transactions* **2009**, *39*, 8280−8291.
(27) Balachandran, P. V.; Rajan, K.; Rondinelli, J. M. Electronically driven structural transitions in $A_{10}(PO_4)_2$ apatites (A = Ca, Sr, Pb, Cd and Hg). *Acta Crystallogr., Sect. B: Struct. Sci.* **2014**, *70* (3), 612−615.
(28) Tate, M. L.; Fuller, C. A.; Avdeev, M.; Brand, H. E. A.; McIntyre, G. J.; Radosavljevic Evans, I. Synthesis and characterisation of new Bi(III)-containing apatite-type oxide ion conductors: the influence of lone pairs. *Dalton Transactions* **2017**, *46* (37), 12494−12499.
(29) Pramana, S. S.; Klooster, W. T.; White, T. J. Framework 'interstitial' oxygen in $La_{10}(GeO_4)_5(GeO_5)O_2$ apatite electrolyte. *Acta Crystallogr., Sect. B: Struct. Sci.* **2007**, *63*, 597−602.
(30) Tate, M. L.; Blom, D. A.; Avdeev, M.; Brand, H. E. A.; McIntyre, G. J.; Vogt, T.; Evans, I. R. New apatite-type oxide ion conductor, $Bi_2La_8[(GeO_4)_6]O_3$: Structure, properties, and direct imaging of low-level interstitial oxygen atoms using aberration-corrected scanning transmission electron microscopy. *Adv. Funct. Mater.* **2017**, *27* (8), 1605625.
(31) Mantid Project. https://www.mantidproject.org/Main_Page (accessed 04/11/2019).
(32) Soper, A. K. *GudrunN and GudrunX*; 2012.
(33) Tucker, M. G., personal communication. 2017.
(34) Lorch, E. Neutron diffraction by germania, silica and radiation-damaged silica glasses. *J. Phys. C: Solid State Phys.* **1969**, *2* (2), 229.
(35) Coelho, A. A.; Evans, J. S. O.; Evans, I. R.; Kern, A.; Parsons, S. The TOPAS symbolic computation system. *Powder Diffr.* **2011**, *26* (4), S22.
(36) Rietveld, H. M. A profile refinement method for nuclear and magnetic structures. *J. Appl. Crystallogr.* **1969**, *2*, 65.
(37) Pramana, S. S.; Klooster, W. T.; White, T. J. A taxonomy of apatite frameworks for the crystal chemical design of fuel cell electrolytes. *J. Solid State Chem.* **2008**, *181* (8), 1717−1722.
(38) Dinnebier, R. E.; Leineweber, A.; Evans, J. S. O. Rietveld Refinement, Practical Powder Diffraction Pattern Analysis using TOPAS. De Gruyter, 2018.
(39) Keen, D. A. A comparison of various commonly used correlation functions for describing total scattering. *J. Appl. Crystallogr.* **2001**, *34* (2), 172−177.
(40) Tucker, M. G.; Keen, D. A.; Dove, M. T.; Goodwin, A. L.; Hui, Q. RMCProfile: reverse Monte Carlo for polycrystalline materials. *J. Phys.: Condens. Matter* **2007**, *19* (33), 335218.
(41) Momma, K.; Izumi, F. VESTA 3 for three-dimensional visualization of crystal, volumetric and morphology data. *J. Appl. Crystallogr.* **2011**, *44* (6), 1272−1276.
(42) Campbell, B. J.; Stokes, H. T.; Tanner, D. E.; Hatch, D. M. ISODISPLACE: a web-based tool for exploring structural distortions. *J. Appl. Crystallogr.* **2006**, *39*, 607−614.
(43) Peet, J. R.; Piovano, A.; Johnson, M. R.; Evans, I. R. Location and orientation of lone pairs in apatite-type materials: a computational study. *Dalton Transactions* **2017**, *46* (46), 15996−15999.
(44) Busing, W. R.; Levy, H. A. The effect of thermal motion on the estimation of bond lengths from diffraction measurements. *Acta Crystallogr.* **1964**, *17* (2), 142−146.
(45) Panchmatia, P.; Orera, A.; Rees, G.; Smith, M.; Hanna, J.; Slater, P.; Islam, M. Oxygen defects and novel transport mechanisms in apatite ionic conductors: combined O-17 NMR and modeling studies. *Angew. Chem., Int. Ed.* **2011**, *50* (40), 9328−9333.
(46) Peet, J. R.; Chambers, M. S.; Piovano, A.; Johnson, M. R.; Evans, I. R. Dynamics in Bi(III)-containing apatite-type oxide ion conductors: A combined computational and experimental study. *J. Mater. Chem. A* **2018**, *6*, 5129−5135.
(47) Addison, A. W.; Rao, T. N.; Reedijk, J.; van Rijn, J.; Verschoor, G. C. Synthesis, structure, and spectroscopic properties of copper(II) compounds containing nitrogen−sulphur donor ligands; the crystal and molecular structure of aqua[1,7-bis(N-methylbenzimidazol-2′-yl)-2,6-dithiaheptane]copper(II) perchlorate. *J. Chem. Soc., Dalton Trans.* **1984**, No. 7, 1349−1356.

DOI: 10.1021/acs.inorgchem.9b02544
Inorg. Chem. 2019, 58, 14853−14862